Chemical Engineering Science 78 (2012) 226–235

Contents lists available at SciVerse ScienceDirect

Chemical Engineering Science

journal homepage: www.elsevier.com/locate/ces

Critical assessment of two approaches for evaluating contacts between super-quadric shaped particles in DEM simulations

G. Lu, J.R. Third, C.R. Müller*

ETH Zürich, Department of Mechanical and Process Engineering, Institute of Energy Technology, Laboratory of Energy Science and Engineering, Leonhardstrasse 27, 8092 Zürich, Switzerland

HIGHLIGHTS

- Two methods to describe super-quadric particles in DEM simulations are investigated.
- The use of discrete points to represent particle surfaces in the DEM is demonstrated.
- The efficiencies of discrete and continuous shape representations are comparable.
- Particle shape has a significant impact on the particle motion in rotating cylinders.

ARTICLE INFO

Article history:
Received 24 December 2011
Received in revised form
16 April 2012
Accepted 24 May 2012
Available online 4 June 2012

Keywords:
Powder technology
Particle
Granular materials
Computation
Rotating cylinder
Discrete element method (DEM)

ABSTRACT

Discrete element method simulations of super-quadric shaped particles have been performed by describing the particles using either a continuous function representation (CFR) or as an array of discrete points (discrete function representation, DFR). For the DFR, techniques of uniform discretization and adaptive discretization were proposed for spherical and non-spherical particles, respectively. The concept of a 'contact candidate list' was put forward to speed up the stage of contact detection. For the CFR, a numerical approach was described to determine the contact point between colliding particles. Points generated through the DFR were used to make the initial guess for the numerical, Newton–Raphson based iterations. The proposed algorithms were employed to model hoppers, horizontal rotating cylinders and vibrated beds. By analyzing the dynamics of these systems the number of discrete points required accurately to describe particles using the DFR was determined. The efficiencies of the DFR and the CFR were measured based on the system of a horizontal rotating cylinder. The characteristics of both modeling approaches in granular simulations were highlighted.

1. Introduction

Granular systems can be found in many industrial systems ranging from rotating cylinders in the cement industry to fluidized beds in the petrochemical industry. To run processes efficiently in these reactors the underlying physics of granular systems have to be well understood. Granular systems are typically opaque, making the acquisition of experimental measurement in such a granular system very difficult (Müller et al., 2006, 2007a, 2007b). The discrete element method (DEM) is a modeling approach which allows the investigation of particle dynamics. Excellent reviews of the recent developments and applications of the DEM approach were given by Zhu et al. (2007, 2008). However, despite the large number of reports of numerical investigations, the underlying physics of granular flows are still only poorly understood. This poor understanding can partly be attributed to the fact that most numerical studies have used perfect spheres, although in reality particles are typically of irregular shape (Müller et al., 2008, 2009, 2010). It is unclear whether or not conclusions made based on measurements in systems composed of spherical particles can easily be transferred to real, non-spherical particle systems. Therefore, the development of simulation techniques to model non-spherical particles is crucial for an improved understanding of real particle systems.

To date, different approaches to model non-spherical particles, such as polygon formulation, composite particles, continuous function representation (CFR), discrete function representation (DFR) or sphero-cylinders, have been proposed. In the following these approaches are described in more detail. (1) Polygon formulation: Hogue and Newland (1994) discretized particles of arbitrary shapes in a 2D polar coordinate system using vertices joined by line segments. The particle contact algorithm was

* Corresponding author. Tel.: +41 44 632 3440.
E-mail address: muelchri@ethz.ch (C.R. Müller).

0009-2509/$ - see front matter © 2012 Elsevier Ltd. All rights reserved.
http://dx.doi.org/10.1016/j.ces.2012.05.041

divided into a set of geometric problems. Hogue and Newland (1994) performed simulations of falling dominos and showed very good agreement with experimental measurements. Feng and Owen (2004) proposed an energy-based polygon contact model in which the contact energy is directly proportional to the overlap between particles. The normal contact force was assumed to point in the direction along which the contact energy decreases fastest. Although the method proposed by Feng and Owen (2004) was initially developed for corner–corner contacts, it can be extended easily to more general contact cases. (2) Composite particles: spherical particles can be 'glued' together to compose arbitrarily shaped non-spherical particles. For example, Third et al. (2010a,b) simulated non-spherical particles by gluing together two spheres of different diameters. They applied this approach to investigate the velocity profile within a horizontal rotating cylinder. The velocity profile obtained using non-spherical particles was found to be consistent with the equation proposed by Nakagawa et al. (1993) based on magnetic resonance measurements. In contrast, when spherical particles were simulated a large amount of slip between the cylinder wall and the particles was reported. The number of spheres used to compose non-spherical particles depends on a balance between computational cost and the accuracy of the shape description (Kruggel-Emden et al., 2008). (3) Continuous function representation (CFR): here, a non-spherical particle is represented using an equation. One commonly used function is the so-called super-quadric equation, which for three-dimensional particles can be written as (Barr, 1981):

$$f(x,y,z)=\left(\left(\frac{x}{a_1}\right)^{2/n_2}+\left(\frac{y}{a_2}\right)^{2/n_2}\right)^{n_2/n_1}+\left(\frac{z}{a_3}\right)^{2/n_1}-1 \quad (1)$$

where a_1, a_2 and a_3 are the half-lengths of the particle along the principle axes, and n_1 and n_2 control the particle squareness. n_1 determines the shape of the cross section in the $y-z$ and $x-z$ planes; while n_2 relates to the shape of the cross section in the $x-y$ plane. When a CFR method is employed, non-linear constrained optimization approaches are required to detect and evaluate contacts between particles. The convergence difficulty of this optimization increases dramatically as the squareness of the particles is increased (Cleary et al., 1997). Mustoe and Miyata (2001) employed super-quadrics to determine the effect of particle squareness on the dynamic angle of repose of cubic particles within a 2D horizontal rotating cylinder. Their results indicated that the dynamic angle of repose has an upper limit of approximately 40°. (4) Discrete function representation (DFR): in this method, which was proposed by Williams and O'Connor (1995), the particle surface is represented by a number of discrete points called nodes. It has been argued that DFR might provide an attractive alternative to the approaches described above due to its computational efficiency and because it can be applied to a wide range of particle shapes (Hogue, 1998). The computational load of the DFR approach scales as O(N), where N is the number of nodes describing the surface of the particle. Williams and O'Connor (1999) proposed contact detection algorithms to reduce the computational load to approximately O($\sqrt{N}$). In these algorithms, an object was distinguished at multiple levels, including a bounding sphere, a bounding box, a cellular region and surface facets. The bounding sphere is an orientation invariant approximation of a non-spherical particle, while the bounding box performs better in capturing the aspect ratio of particles. On the subsequent level of cellular regions, the bounding box was further discretized into a number of cells of fixed size along the direction of each coordinate axis. The cells which contained a part of the particle surface were 'marked'. Finally, at the highest resolution of representation using surface facets, the boundary of the particle was approximated by a series of facets, which are lines in 2D and triangles in 3D. (5) Sphero-cylinders: a sphero-cylinder is a cylinder with hemi-spherical ends of the same radius as the cylinder. Contact detection between two sphero-cylinders can be sub-divided into three scenarios: sphere–sphere, sphere–cylinder or cylinder–cylinder contacts. Langston et al. (2004) simulated the discharge of sphero-cylinders from a hopper and found that the aspect ratio of the particles did not have a significant influence on the fraction discharged (defined as the mass of the particles discharged divided by the mass of particles initially in the hopper).

So far, the most common approaches of modeling non-spherical particles have been the use of polygon-shaped particles or the construction of particles as composites of spheres. Contact detection algorithms for the polygon based approach must consider separately contacts involving vertices, edges or faces. As a result these algorithms are often complex and time-consuming. The composite particles approach results in a high computational load in case that a large number of spheres is used to model a smooth, non-spherical particle. In addition, it has been demonstrated that if more than one sphere is involved in a contact, the 'common' force models have to be modified to prevent an over-stiff or over-damped force-deflection response (Kodam et al., 2009). Reports of simulations of industrial and geophysical particle flows performed using a CFR modeling approach (Cleary, 2010) remain relatively scarce. Regarding the DFR, certain aspects related to this technique have to be addressed: (1) How can a particle be discretized conveniently? (2) How many points are required to discretize a particle to guarantee sufficient resolution? (3) How should the discretized points be distributed on the surface of a particle? (4) How can the contact point be found efficiently based on the discretized points? (5) How shall the contact point and the contact normal be determined? In addition, the computational efficiencies of both the CFR and DFR have to be evaluated *via* benchmark simulations.

In this work we focus on convex particle shapes and examine the feasibility of the CFR and the DFR schemes using typical granular systems as test cases. We also aim to highlight the advantages and disadvantages of the two modeling techniques.

2. Simulation methods

2.1. Basic concepts of DEM for non-spherical particles

The principles of DEM are well documented in the literature (Zhu et al., 2007) and will not be repeated except to detail the force laws adopted in this work. In the normal direction, a damped linear spring model was implemented and attractive forces between colliding particles were prevented. The contact force in the normal direction was given by

$$F_n=\max\left(0,k_{n_{ij}}\delta_n-2\eta_n\sqrt{m_{ij}k_{n_{ij}}}v_n\right) \quad (2)$$

Here δ_n is the overlap between the colliding particles, η_n is the damping factor in the normal direction, v_n is the relative velocity in the normal direction, m_{ij} is the effective mass given by $1/m_{ij}=1/m_i+1/m_j$ and $k_{n_{ij}}$ is the effective normal stiffness defined as $1/k_{n_{ij}}=1/k_{n_i}+1/k_{n_j}$. In the tangential direction, the friction force was modeled as a damped linear spring, and its magnitude was limited by Coulomb's law, such that:

$$F_t=\min\left(\mu k_{n_{ij}}\delta_n,k_{t_{ij}}\delta_t-2\eta_t\sqrt{m_{ij}k_{t_{ij}}}v_t\right) \quad (3)$$

where μ is the coefficient of friction, η_t is the damping factor in the tangential direction, and v_t is the relative velocity in the tangential direction. The tangential displacement was calculated

according to $\delta_t = \int v_t \, dt$ and the effective tangential stiffness is defined as $1/k_{t_{ij}} = 1/k_{t_i} + 1/k_{t_j}$.

In this work we consider spherical particles and non-spherical particles, the surface of which was described by the super-quadric equation (1). The contact detection algorithm for super-quadric particles can be divided into two steps: contact detection and contact evaluation. The first stage of contact detection is to perform a neighbor search by approximating the particles as their bounding spheres, which are concentric with the super-quadric particles. The radius R of the bounding sphere is based on the particle's half-lengths and is given by $R = \sqrt{a_1^2 + a_2^2 + a_3^2}$. Next, a bounding box, with the center and the principle axes coincident with those of the super-quadric particle, is employed to identify the contact. Often the bounding sphere is only a rough approximation of the super-quadric particle. In particular for particles with a large aspect ratio, a bounding box is necessary to rule out contacts for which the bounding spheres overlap but the two particles are still far away from each other due to their shapes and orientations. In the contact evaluation step the contact parameters, i.e. the contact point and the contact normal, are established. Owing to its computational efficiency, the geometric potential approach (Lin and Ng, 1995; Houlsby, 2009) is used to define the contact point. Fig. 1, showing a two-dimensional contact between two ellipses, illustrates the determination of the contact parameters. First, the point on the surface of particle 1 which has the lowest geometric potential energy relative to particle 2 is located. In the following we shall denote this point P_1. Subsequently, it is determined whether P_1 lies inside particle 2. For example, if $f_2(x_1,y_1,z_1) < 0$, where x_1, y_1 and z_1 are the coordinates of P_1 and f_2 is the super-quadric equation of particle 2, particle 1 is in contact with particle 2. Note that the same process must also be performed for particle 2 to identity the point on its surface that has the lowest geometric potential energy relative to particle 1. We denote this point P_2. Finally, the following procedures are performed to calculate the overlap and the contact normal: (1) compare the geometric potential energies of the two points P_1 and P_2 and determine the point which possesses the lowest potential energy. In the following it is assumed that P_2 has a lower potential energy than P_1. (2) Calculate the contact normal as the surface normal at P_2. (3) Connect P_1 and P_2 and project this line onto the contact normal to calculate the contact overlap. (4) The contact point is defined as the position obtained by adding a vector corresponding to half of the overlap in the normal direction to P_2.(5) Determine the contact forces according to Eqs. (2) and (3). In Fig. 1, the dot in the central part of the penetration zone represents the contact point, and the numbers on the dashed ellipses are the geometric ratio between the dashed lines and the real particle surface (solid ellipses).

The definition of the contact point described above requires a method to locate the point on a particle's surface which has the lowest geometrical potential energy with respect to another particle. In this work this problem is solved either by representing the surface of a particle by a number of discrete points or by using the super-quadric equation.

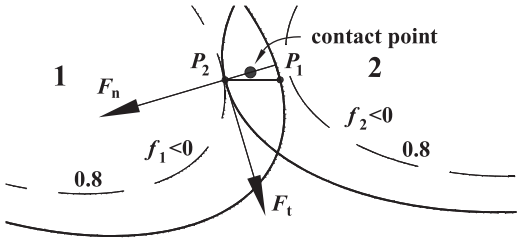

Fig. 1. Definition of the overlap and the contact normal of super-quadric particles based on the geometric potential concept.

2.2. Contact resolution based on the discrete function representation (DFR)

The DFR approach requires two steps: (1) the discretization of the surface of a particle using a sufficient number of points to allow contacts between particles to be modeled accurately and (2) the computationally efficient determination of the point of lowest geometric potential energy.

Depending on the particle shape, two different approaches were proposed for the first task. (i) Uniform discretization: here points are uniformly distributed on the surface of a particle. This strategy is most suited to particles that are approximately spherical. In our method, the number of points on the equator of a sphere is used to control the distance between neighboring points. Points along the north–south and the east–west directions are generated based on the appointed spacing along the equator, leading to equally spaced points in these two directions. Fig. 2(a) shows an example of such a discretized sphere using 40 points on the horizontal equator. (ii) Adaptive discretization: this strategy can be applied to convex particles described by the super-quadric equation. Normally the contact resolution relies on two factors, namely the total number of points used to discretize a particle and the distribution of points over the surface of a particle (Hogue, 1998). Here, a new method was developed to meet the requirement of accurate contact detection. First, a bounding box is drawn around the particle. The bounding box is a cuboid with side lengths equal to twice the half-lengths of the particle. Next, points are generated on the edges of this bounding box. The number of points and the smallest spacing between neighboring points are set in advance. Subsequently, the distance between neighboring points is regulated following a linear rule along the direction from the vertex of the bounding box to the mid-point of its edge. Thus, the density of the points can be adjusted according to the local curvature of a particle's surface. After that, the positions of the points on the surface of the bounding box, i.e. the intersections of lines which are perpendicular to the edges and pass through the points on the edges, are determined. Finally, the points created are mapped onto the actual surface of the particle by determining the intersection point between the particle's super-quadric equation and a line passing through the center of the particle and the point on the bounding box. Fig. 2(b) shows an example of such a discretized super-quadric particle (squareness parameters $n_1 = n_2 = 0.4$ and half-length 0.001 m). The points are generated based on setting 20 points on each edge of the bounding box.

For the second task, i.e. the determination of the point of the lowest geometric potential energy, a new concept termed 'contact candidate list' that avoids searching the whole array of nodes at each time step, is proposed here. In this method each node, P, has a list associated with it, which contains the nodes that are closest to P (including P itself). This list is arranged in ascending order of the straight line distance between the nodes and P. The aim of this concept is to narrow the search for the point of lowest geometric potential energy at the current time step using the information from the previous time step. Since the time step of DEM simulations is very small and the positions and the orientations of the particles do not change significantly in this short period, it can be anticipated that the point of lowest geometric potential energy will not move a substantial distance from one time step to another. In this work the length of the contact candidate list is set to be 10. For the discretization schemes employed here, this ensures that the contact candidate list of a point contains all of the points that are its direct neighbors. The point of lowest geometric potential energy is determined as the point which has a lower geometric potential than any of the points on its contact candidate list. To find this point we first compare the

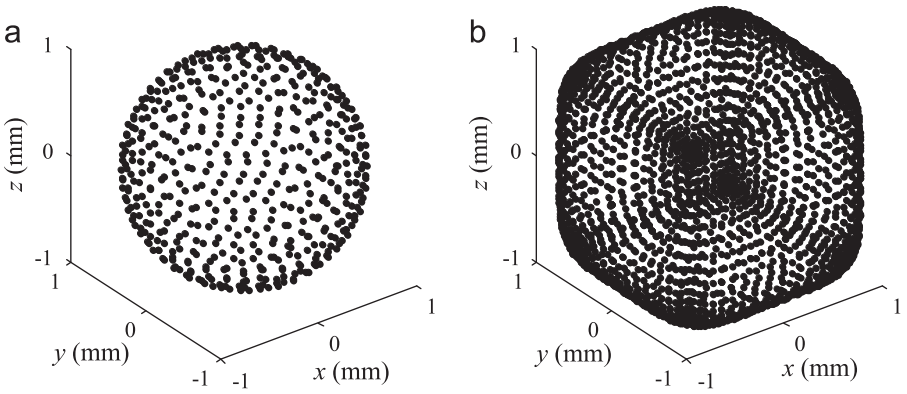

Fig. 2. Discrete function representation of particles through uniform discretization and adaptive discretization: (a) spherical particle (uniform discretization) and (b) super-quadric particle (adaptive discretization).

energy of the geometric potential point G_1 obtained at the previous time step with those of the other points in the contact candidate list of G_1. If G_1 has the lowest geometric potential energy then it is the point of lowest geometric potential of the current time step. Otherwise we move to point, G_2, which has the lowest geometric energy of the points on the contact candidate list of G_1. To reduce the computational load, the points that have been searched but were found to have a higher geometric potential energy than G_2 are 'marked' to indicate that they do not need to be re-searched. Subsequently, we check the points in the contact candidate list of G_2 that have not been marked to identify the point of lowest geometric potential energy. This process is repeated until the point is found which has the lowest geometric potential energy compared to the other points in its contact candidate list. Since the shape of the particles investigated here is convex, it is guaranteed that the final point obtained using the above described method has the lowest geometric potential energy. The minimum length of the contact candidate list for this method only depends on the particle discretization approach used. In this work the DFR approach using the 'contact candidate list' method was employed.

2.3. Contact resolution based on the continuous function representation (CFR)

In the CFR approach, numerical optimization techniques are employed to solve for the point of lowest geometric potential energy of contacting particles. An auxiliary potential function is established as

$$\Pi = f_1(x,y,z) + \lambda f_2(x,y,z) \tag{4}$$

Here f_1 and f_2 are the super-quadric equations of particle 1 and particle 2, respectively, and λ is the Lagrange multiplier. Π is minimized with respect to the variables x, y, z and λ. That is, we solve for a point which is on the surface of particle 2 and has the lowest geometric potential energy relative to particle 1, and vise versa.

The Newton–Raphson approach is used to solve numerically the set of equations described above. The DFR approach described previously is used to provide an initial guess for x, y, z and λ. Suppose that a set of points is generated on the surface of a particle. On the initial contact moment, when the bounding boxes of two particles are in contact, all the points on one particle are checked to determine the point of lowest geometric potential energy relative to the other particle. The coordinates of this point are then used as the first guess for the Newton–Raphson method. In the work proposed here we used 26 points as the basis for the first guess. These points include the vertices and the centers of the faces and the edges of the super-quadric particle, as shown in Fig. 3. A fixed value is used as the initial estimate of λ. For the subsequent time steps, the solutions of the Newton–Raphson method obtained from the previous time step are used as the initial guess.

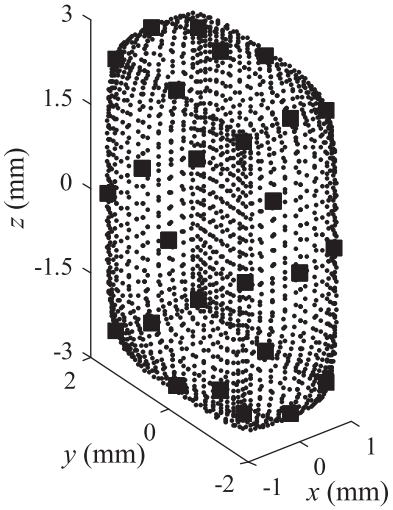

Fig. 3. Points on the surface of a super-quadric particle that provide the initial guess for the Newton–Raphson iterations.

3. Results and discussion

The DEM algorithms described above were validated by performing benchmark simulations of granular flows composed of either spherical or non-spherical particles. We consider three systems: hopper, vibrated bed and horizontal rotating cylinder.

3.1. Simulations of spherical particles

First, we study the discharging behavior of a 3D hopper of rectangular cross-section. The dimensions of the hopper are 0.12 m × 0.03 m × 0.16 m in terms of length × width × height. In total, 12,000 spherical particles of average diameter 3 mm (the particle size distribution is ±5% of the average diameter) are generated inside the hopper with random initial velocities and are allowed to settle under gravity. The density of the particle used is 2500 kg/m^3, the stiffness is 2000 N/m and the damping factors in the normal and tangential directions are chosen as 0.22 and 0.2, respectively. The coefficient of friction for both particle–particle

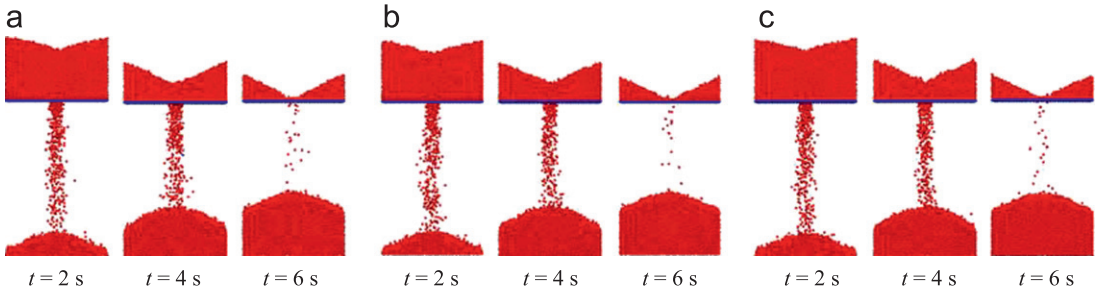

Fig. 4. Snapshots of the discharge of spherical particles from a hopper of rectangular cross-section: (a) 'standard' DEM for spherical particles; (b) 200 points on the equator of a sphere using the DFR approach and (c) the CFR approach.

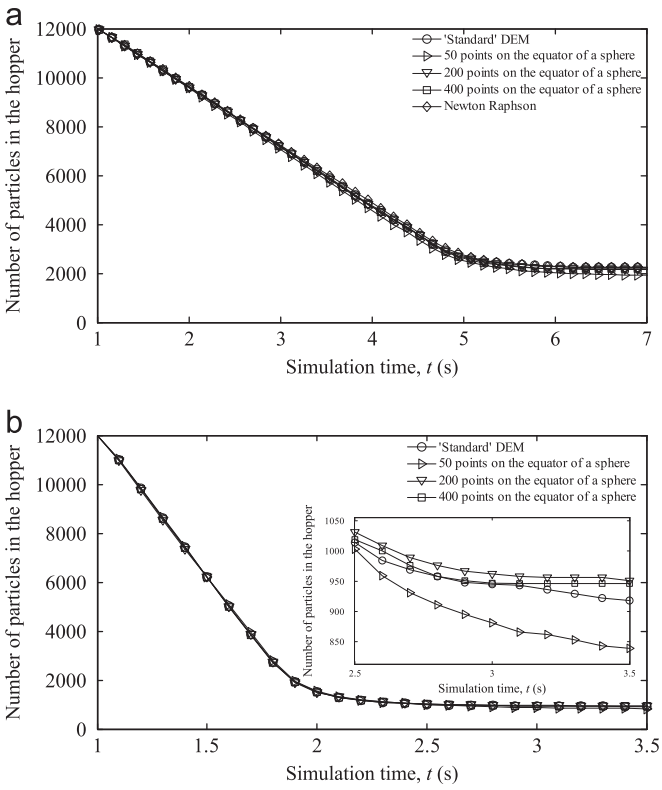

Fig. 5. Discharge curves for hoppers containing 12,000 spherical particles simulated using the 'standard' DEM, the DFR and the CFR approaches: (a) hopper with a small orifice and (b) hopper with a large orifice.

and particle–wall contacts is set to 0.7. Discharge of the hopper is initiated by opening a square orifice of length 0.018 m (six times of the average particle diameter) in the center of its base. Simulations were performed using the 'standard' DEM, the DFR approach using 50, 200 or 400 points on the equator of a sphere (corresponding to 835, 12,779 or 51,026 points on the surface of a sphere in total), and the CFR approach. Fig. 4 shows selected snapshots of the particle positions during hopper discharge simulated using the three different modeling techniques.

From the snapshots shown in Fig. 4 it can be seen that the three modeling techniques predict that a 'V'-shaped wedge of material remains in the hopper after discharge. The angle of this 'V'-shaped geometry is the angle of repose of the spheres. The change in the number of particles within the hopper with time is plotted in Fig. 5(a). From Fig. 5(a) it can be seen that the DFR simulation employing 50 points on the equator of a sphere leads to a faster discharging rate, whereas the curves for the DFR approach using a larger number of nodes are very close to each other and are in good agreement with the 'standard' DEM. These data suggest that, for the spherical particles used here, representing the particles using 200 points on the equator is sufficient to capture the particulate behavior accurately. In addition, the CFR approach gives very good agreement with the 'standard' DEM. To assess the significance of the results presented in Fig. 5(a), each simulation was performed a further four times using different initial conditions (initial particle velocities). We test the null hypothesis, H_0, that there is no statistically significant difference between the results obtained using the DFR with 50 points on the equator and the 'standard' DEM. It is assumed that the results produced by both the 'standard' DEM and the DFR with 50 points on the equator are normally distributed. It is anticipated that the variance of the two modeling approaches may be different so H_0 will be evaluated using a two-tailed Welch's T-test. The analysis was performed based on the number of particles remaining in the hopper after 7 s of simulated time and a significance level of 1% shall be adopted. For the 'standard' DEM the mean number of particles remaining in the hopper was 2195.8 and the standard deviation was 39.52. The DFR with 50 points on the equator gave a mean of 1941.6 and a standard deviation of 34.11. The sample size is 5 for both simulation methods. Assuming H_0, the probability of obtaining a discrepancy at least as large as the observed discrepancy is approximately 1×10^{-5}. Therefore there is evidence to reject H_0 at the 1% significance level.

In order to test whether the size of the orifice has an influence on the number of points required accurately to represent a sphere, simulations with a larger orifice (0.06 m × 0.018 m) were performed. Fig. 5(b) compares the discharge behavior of particles discretized by a different number of points. Since the orifice is enlarged, the flow rate is greatly increased. The inset in Fig. 5(b) shows the deviation between the different DFR approaches in more detail. Following the methodology described above, each of the simulations for the large orifice size was performed five times with different initial conditions. The mean number of particles remaining in the hopper after 3.5 s of simulated time was found to be 919 for the 'standard' DEM and 844.8 for the DFR with 50 points on the equator of a sphere. The standard deviations were, respectively, 20.6 and 7.4. A two-tailed Welch's T-test with 1% significance has been applied to these data to assess the null hypothesis stated above. This analysis predicted that the probability of obtaining a discrepancy at least as large as the observed discrepancy if H_0 were true would be approximately 1×10^{-3}. Consequently, there is evidence to reject H_0 at the 1% significance level. Thus, the system with enlarged orifice dimensions also requires 200 points on the equator of a sphere to model its discharge dynamics accurately.

As a second test case, the particle motion inside a horizontal rotating cylinder was investigated. The length and diameter of the cylinder were 0.152 m and 0.1 m, respectively (Third et al., 2010a,b). The cylinder contains 11,220 spherical particles of average diameter 3 mm (the particle size distribution is ±5% of the average diameter), corresponding to a fill level of

approximately 26%. Here, the fill level is defined as the fraction taken up by the particles and the voids between particles while the cylinder is rotating. Wall rougheners are employed to suppress the slip between the particles and the cylinder wall. The wall rougheners are composed of spherical particles of diameter 3 mm, running along the direction of the cylinder axis. In total 52 equally spaced lines of wall rougheners are created around the cylinder circumference. The centers of the spheres making up the wall rougheners are located on the surface of the cylinder. Fig. 6(a) shows a typical snapshot of the cylinder investigated. To quantify the particle motion within the cylinder, the velocity profile along a radius perpendicular to the free surface of the bed (tangential velocity profile, TVP) was calculated. The TVP shows the spatially resolved average particle velocity parallel to the surface of the bed for particles located in a narrow section between the dashed lines *AB* and *CD* marked in Fig. 6(b). The system operates in the rolling mode with a rotation speed of 10 rpm, thus the dynamic angle of repose, θ, is given by the angle between the surface of the bed and the horizontal line. After initialization of the cylinder rotation, 10 s was allowed for the system to reach steady state. The rate of axial dispersion can be reflected by the mean square deviation of particle positions along the axial direction of a cylinder, namely $\sum_{k=1}^{tot}(z_k(t)-z_k(0))^2/tot$, where z_k is the axial position of a particle k and tot is the total number of particles considered. The mean square deviation of particle positions is calculated using the particle positions between 10 s and 100 s, using 10 s as a time segment. In order to prevent the influence of end plates due to the finite axial length of a cylinder, the analysis is restricted to particles in a pulse centered half way along the cylinder. Here, the length of the pulse is chosen as 10 cm, which was demonstrated to be free from the end plates restriction for the time range considered (Third et al., 2010a,b). Simulations were performed using the 'standard' DEM for spherical particles, the DFR approach using 50, 100 or 200 points on the equator of a sphere and the CFR approach.

To calculate the dynamic angle of repose, we divide the cylinder into 10 sections of equal width, as shown in Fig. 6(b). For each section, the particle with the highest y coordinate is identified. The free surface of the bed is approximated by fitting a straight line through the coordinates of the particles selected in this way. The dynamic angle of repose is calculated as the angle formed between this line and the x-axis. The dynamic angles of repose, averaged over 90 s, are 28.2°, 24.9°, 28.1°, 28.1° and 28.2° for the 'standard' DEM, the DFR using 50, 100 and 200 points on the equator of a sphere and the CFR, respectively. Results obtained for the TVP and for the mean square deviation in the axial positions of the particles are shown in Fig. 7. In the active region, i.e. near the surface of the particle bed, negative velocities are encountered; whereas the particles close to the cylindrical wall have positive velocities. Turning now to the axial dispersion rates, all simulations indicate that the mean square deviation in the axial positions of the particles increased linearly with time, thus following Fick's second law. For both dynamic properties of a rotating cylinder, the DFR approach using 50 points on the equator of a sphere is insufficient to model the particles accurately. The axial dispersion coefficient predicted using 50 points on the equator of a sphere is 2.45×10^{-6} m^2/s and the standard deviation between different time segments is 7.57×10^{-8} m^2/s.

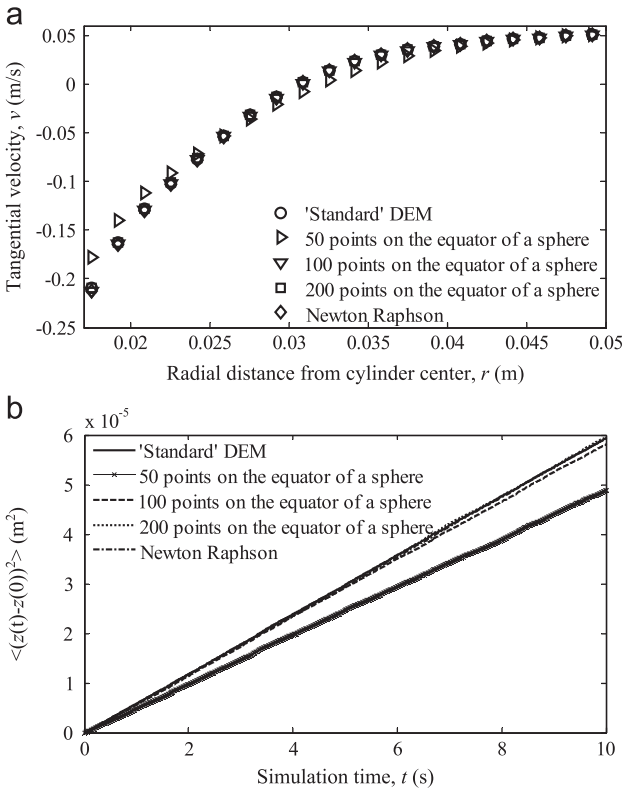

Fig. 7. Comparison of tangential velocity profiles and rates of axial dispersion of 11,220 spherical particles within a horizontal, rotating cylinder based on the 'standard' DEM, the DFR and the CFR: (a) tangential velocity profiles and (b) rates of axial dispersion.

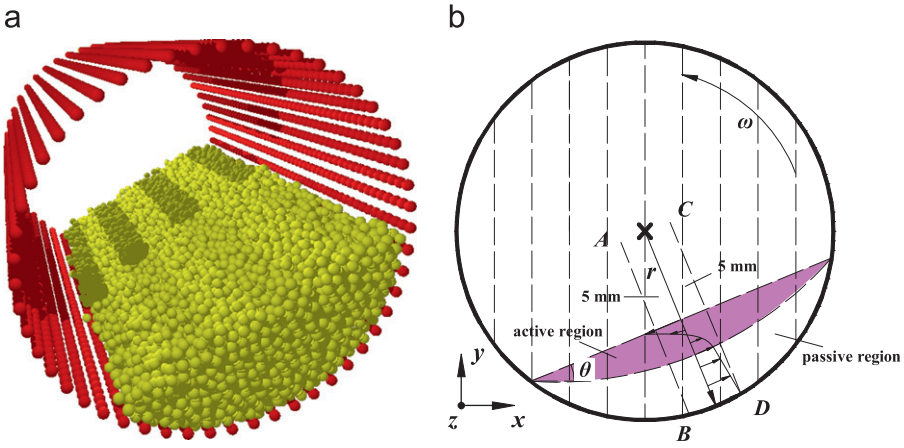

Fig. 6. (a) Configuration of a horizontal rotating cylinder containing spherical particles; (b) schematic drawing showing the sample particles chosen for the calculation of tangential velocity profile (TVP).

For the 'standard' DEM, the mean axial dispersion coefficient is 2.97×10^{-6} m^2/s and the standard deviation is 3.4×10^{-8} m^2/s. Increasing the number of points to 100 on the particle equator, however, gives very good agreement with the 'standard' DEM approach. The TVP predicted using 100 discrete points on the equator of a sphere is indistinguishable from the TVP calculated by the 'standard' DEM and the error in the axial dispersion coefficient, D_{ax}, is only 2%, which is less than the standard deviation between different time segments. Using the CFR the simulation results are indistinguishable from those obtained using the 'standard' DEM.

3.2. Simulations of non-spherical particles

The DEM algorithms proposed here are further validated using non-spherical particle systems. Using the DFR and CFR methods the dynamics of cubic particles in a horizontal, rotating cylinder were studied. The characteristic dimensions of the system are identical to those used for spheres. The cylinder contained 11,220 cubic particles with squareness parameters $n_1 = n_2 = 0.4$. The length of the principal axis is 2.42 mm, resulting in a cube of equal volume to the spheres simulated previously. The particle size distribution is $\pm 5\%$ of the average length. The fill level of the cylinder is approximately 25.8%, which is very similar to the fill level of the system containing spheres. Wall rougheners are not employed since the non-sphericity of the particles significantly reduces the slip between the particles and the cylinder wall. Fig. 8(a) gives a snapshot of the system simulated. Simulations were performed based on the DFR using 10, 20, 40 or 60 points on the edge of a cube, which corresponds to, respectively, 602, 2402, 9602 or 21,602 points in total. Simulations were also performed using the CFR method. For the DFR an inhomogeneous distribution of points is employed such that more points are generated around the particle's vertices. The cylinder is rotated with a speed of 10 rpm. The system is allowed to reach a steady state during the initial 11 s. From time 11 to 60.5 s, subsequent time segments of 5.5 s length are averaged to calculate the rate of axial dispersion.

In addition, the dynamic angle of repose, based on the simulation data from time 11 to 60.5 s, was calculated using the procedure introduced previously for spherical particles. The angles of repose obtained are 34.9°, 38.1°, 36.2°, 36.2° and 35.9° for the DFR using 10, 20, 40 or 60 points on the edge of a cube and the CFR, respectively. The tangential velocity profiles and the rates of axial dispersion obtained are shown in Fig. 8(b) and (c). With regards to the rate of axial dispersion, all simulations show that the mean square deviation of the axial position of the particles increased linearly with time, thus following Fick's second law. However, from both Fig. 8(b) and (c) it is clear that the DFR method using 10 points on the edge of a cube is insufficient to model the particles accurately. The simulation results for both the tangential velocity profile and the rate of axial dispersion deviate significantly from the other simulation results. The axial dispersion coefficient predicted using 10 points on the edge of a cube is 3.38×10^{-6} m^2/s and the standard deviation between different time segments is 1.67×10^{-7} m^2/s. This is substantially smaller than the dispersion coefficients predicted by the other simulations. For example, the CFR approach gave a dispersion coefficient of 5.7×10^{-6} m^2/s and a standard deviation of 1.67×10^{-7} m^2/s. Using 20 points on the edge of a cube provides a good prediction of the rate of axial dispersion, but fails to predict satisfactorily the tangential velocity profile. However, increasing the number of points on the edge of a cube to 40 appears to be sufficient to predict the TVP accurately. On the other hand, the results of the CFR approach agree very well with the simulation results obtained from the DFR method using a sufficient number of points. An interesting result

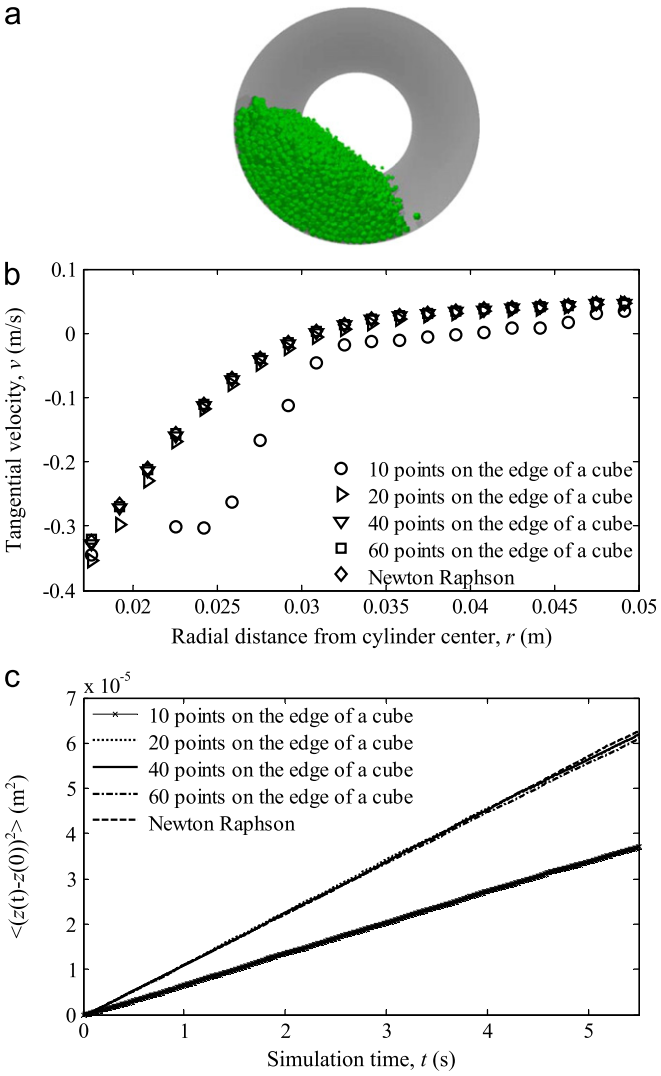

Fig. 8. (a) Configuration of a horizontal rotating cylinder containing cubic particles; (b) comparison of tangential velocity profiles of 11,220 cubic particles within a horizontal rotating cylinder based on the DFR and the CFR; (c) comparison of rates of axial dispersion of 11,220 cubic particles within a horizontal rotating cylinder based on the DFR and the CFR.

of this simulation is that the rate of axial dispersion of cubic particles is approximately 1.9 times larger than that of spherical particles of the same volume. The underlying physics for this faster transportation of non-spherical particles along the axial direction of a horizontal rotating cylinder will be addressed in a separate study.

Finally, a 2D vibrated bed with dimensions 0.1 m × 0.15 m (width × height) was simulated. In total 2000 square particles were generated with squareness parameters $n_1 = n_2 = 0.5$ and average length 1 mm along the principal axis, leading to a dimensionless filling height (defined as the actual height of the bed divided by the average length of the particle used) of approximately 20. A particle size distribution of $\pm 10\%$ of the average length was employed. Here, we change the squareness parameters of particles used in the previous simulation to evaluate the performances of the proposed DEM algorithms on a different non-spherical shape. The bed is vibrated with a frequency $B = 20$ Hz and an amplitude $A = 0.0043$ m, resulting in a dimensionless acceleration parameter of $\Gamma = A(2\pi B)^2/g = 7.0$. The density of particles is 2500 kg/m^3, and their stiffness is 10,580 N/m. The coefficients of restitution and friction (particle–particle and particle–wall) are set to 0.8 and 0.1, respectively.

Simulations were conducted using the CFR approach and the DFR approach with 6, 10, 20, 40 or 60 points on the edge of a cube (corresponding to 24, 40, 80, 160 or 240 points in total, respectively). The dynamics of the vibrated bed are determined 10 s after the start of the simulation. Simulation data obtained from 10 to 60 s are used to calculate the probability density functions of the particle velocities.

Fig. 9(a) shows snapshots of the vibrated bed during a vibrating cycle. The formation of surface waves can be seen clearly. The frequency of the waves is one quarter of the external driving frequency. In order to evaluate the accuracy of the different modeling approaches, a statistical analysis of the horizontal and vertical velocities of the particles, based on a 50 s time segment, was performed. The probability density functions of the horizontal and vertical velocities are plotted in Fig. 9(b) and (c), respectively. From Fig. 9(b) it can be seen that the distributions of velocities in the x-direction are symmetric around $v_x = 0$ m/s. The velocities lie mostly in the range of ± 0.4 m/s. Combined with Fig. 9(c), it was found that using the DFR approach with six points on the edge of a cube is not sufficient to predict the dynamics of the system accurately. If the number of points is increased to 10, the probability density function of particle velocities in the vertical direction is in good agreement with those predicted using a large number of points. However, in the probability density function of the velocities in the horizontal direction a large deviation can still be observed. For example, the simulation with 10 points on the edge of a cube predicts that the fraction of particles having horizontal velocities in the range $-0.04\ \text{m/s} < v_x < -0.02\ \text{m/s}$ is 0.0677, while the CFR approach predicts 0.06. To allow the significance of this discrepancy to be estimated, probability densities have also been calculated by dividing the simulated time into five time segments of 10 s. The standard deviation between those time segments for the fraction of particles with horizontal velocities in the range $-0.04\ \text{m/s} < v_x < -0.02\ \text{m/s}$ was found to be 8.2×10^{-4} for the simulation with 10 points on the edge of a cube, and 9.75×10^{-4} for the CFR. This inconformity can be eliminated by increasing further the number of points on the edge of a cube to 20. The numerical results obtained using the CFR method are very close to the predictions of the DFR methods using a sufficiently large number of points.

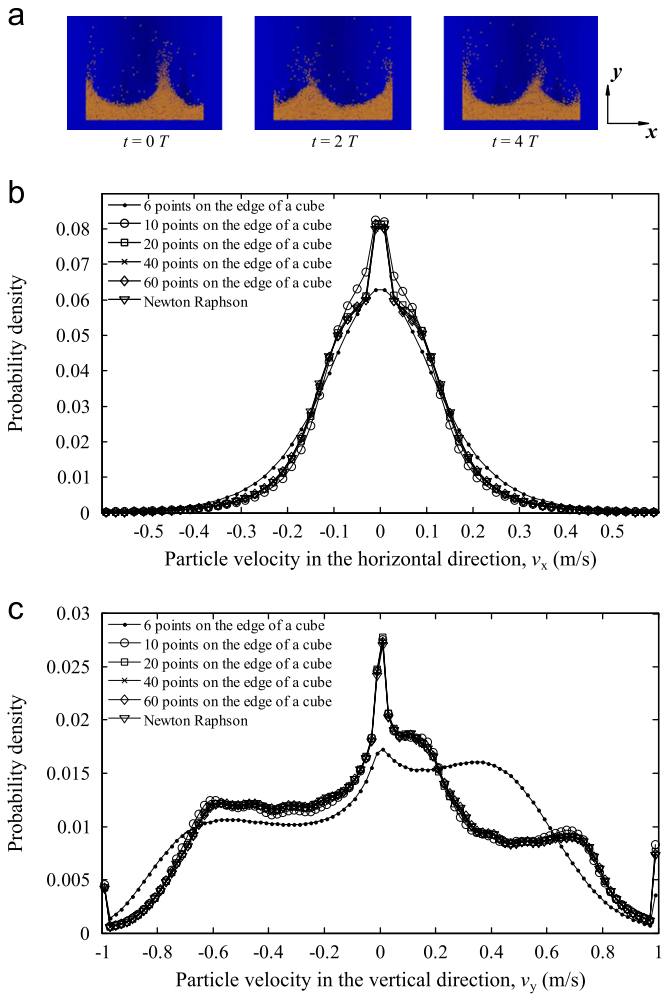

Fig. 9. (a) Snapshots of $f/4$ waves formed by 2000 cubic particles inside a 2D vibrated bed; (b) probability density of particle velocities in the horizontal direction based on the DFR and the CFR; (c) probability density of particle velocities in the vertical direction based on the DFR and the CFR.

3.3. *Efficiency test on the DFR and CFR*

To evaluate the efficiencies of the DFR and CFR approaches, benchmark simulations that are based on the horizontal, rotating cylinder described above have been performed. The cylinder contains 11,220 particles and tests have been performed using either spherical or non-spherical particles. For spherical particles wall rougheners are employed and the simulations are run until 10 s of rotation have been simulated. For non-spherical particles 11 s of rotation is simulated and wall rougheners are not used. The benchmark simulations were performed on a desktop computer running Linux (64 bit). The elapsed system time required by the simulations was recorded automatically and no data were written to the hard disk by the benchmark simulations. Table 1 shows the simulation time obtained under these conditions. These data indicate that, for spherical particles, both the DFR and CFR employed in this work are substantially slower than the 'standard' DEM. The DFR using 100 points on the equator of a sphere has an efficiency of about 20% of the 'standard' DEM, while the DFR using 200 points and the CFR both have efficiencies of approximately 7% of the 'standard' DEM. It was found that for the DFR method the scaling relation between the computational time and the number of points employed to represent a particle is not linear. The data for spherical particles presented in Table 1 suggest that the computational time increases as $N^{0.65}$. The computational load increases significantly when cubic particles are simulated, but the efficiencies of the CFR and DFR remain comparable.

Table 1
Comparison of computational times for a horizontal rotating cylinder simulated using the 'standard' DEM, DFR and CFR approaches.

Particle type	DEM scheme	Simulation time (s)	Elapsed time (h)
Sphere	'Standard' DEM	10	2:18
Sphere	DFR: 100 points on the equator (3203 points in total)	10	11:40
Sphere	DFR: 200 points on the equator (12,779 points in total)	10	28:45
Sphere	CFR	10	35:50
Cube	DFR: 40 points on the edge (9602 points in total)	11	169:16
Cube	CFR	11	150:44

4. Conclusions

Two different approaches to model super-quadric particles using the DEM have been investigated: continuous function representation (CFR) and discrete function representation (DFR). These algorithms have been evaluated through simulations of hoppers, horizontal rotating cylinders and vibrated beds. The main conclusions of this work are as follows.

- For spherical particles there is excellent agreement between simulations performed using the CFR and the 'standard' DEM. The performance of the DFR depends on the number of points used to discretize the particles: good agreement is obtained using 100 points on the equator of a sphere, while the results are indistinguishable from the 'standard' DEM when 200 points are used on the equator.
- For simulations of non-spherical particles there is excellent agreement between the predictions of the CFR and the DFR if a sufficient number of discretizing points are used. The agreement between these two methods suggests that both of these models are able accurately to model the motion of super-quadric particles. For two granular systems containing super-quadric cubes studied here it was found that the DFR required 40 points on the edge of a cube to achieve sufficient contact accuracy.
- While the codes employed in this work have not been fully optimized, the efficiencies of the CFR and DFR appear to be comparable.
- Both continuous function representation and discrete function representation are feasible methods for modeling non-spherical particles using the DEM.

Notation

a_1,a_2,a_3	half lengths of a particle along its principle axes, m
A	vibrating amplitude, m
B	vibrating frequency, Hz
D_{ax}	axial dispersion coefficient, m^2/s
f	super-quadric equation of a particle
F_n	contact force in the normal direction, N
F_t	contact force in the tangential direction, N
G,P	discrete points on the surface of a particle
k_{n_i}	normal stiffness of particle i, N/m
$k_{n_{ij}}$	effective normal stiffness, N/m
k_{n_j}	normal stiffness of particle j, N/m
k_{t_i}	tangential stiffness of particle i, N/m
$k_{t_{ij}}$	effective tangential stiffness, N/m
k_{t_j}	tangential stiffness of particle j, N/m
m_i	mass of particle i, kg
m_{ij}	effective mass, kg
m_j	mass of particle j, kg
n_1,n_2	squareness parameters of a super-quadric particle
N	number of nodes describing the surface of a particle
r	radial distance from cylinder center, m
R	radius of a bounding sphere, m
t	simulation time, s
T	vibrating cycle, s
tot	total number of particles
v	tangential velocity, m/s
v_x	horizontal velocity, m/s
v_y	vertical velocity, m/s
v_n	relative velocity in the normal direction, m/s
v_t	relative velocity in the tangential direction, m/s
x,y,z	coordinates

Greek letters

δ_n	overlap between the colliding particles, m
δ_t	tangential displacement between the colliding particles, m
η_n	damping factor in the normal direction
η_t	damping factor in the tangential direction
Γ	dimensionless acceleration
λ	Lagrange multiplier
μ	coefficient of friction
θ	dynamic angle of repose, $^\circ$
ω	angular velocity of a rotating cylinder, rad/s
Π	auxiliary potential function

Acknowledgments

The authors are grateful to the Swiss National Science Foundation (Grant 200021_132657/1) and the China Scholarship Council for partial financial support of this work.

References

Barr, A.H., 1981. Superquadrics and angle-preserving transformations. IEEE Comput. Graph. Anim. 1, 11–23.
Cleary, P.W., 2010. DEM prediction of industrial and geophysical particle flows. Particuology 8, 106–118.
Cleary, P.W., Stokes, N., Hurley, J., 1997. Efficient collision detection for three dimensional super-ellipsoidal particles. In: Proceedings of Eighth International Computational Techniques and Applications Conference, University of Adelaide, Adelaide.
Feng, Y.T., Owen, D.R.J., 2004. A 2D polygon/polygon contact model: algorithmic aspects. Eng. Comput. 21, 265–277.
Hogue, C., 1998. Shape representation and contact detection for discrete element simulations of arbitrary geometries. Eng. Comput. 15, 374–390.
Hogue, C., Newland, D., 1994. Efficient computer simulation of moving granular particles. Powder Technol. 78, 51–66.
Houlsby, G.T., 2009. Potential particle: a method for modelling non-circular particles in DEM. Comput. Geotech. 36, 953–959.
Kodam, M., Bharadwaj, R., Curtis, J., Hancock, B., Wassgren, C., 2009. Force model considerations for glued-sphere discrete element method simulations. Chem. Eng. Sci. 64, 3466–3475.
Kruggel-Emden, H., Rickelt, S., Wirtz, S., Scherer, V., 2008. A study on the validity of the multi-sphere Discrete element method. Powder Technol. 188, 153–165.
Langston, P.A., Al-Awamleh, M.A., Fraige, F.Y., Asmar, B.N., 2004. Distinct element modeling of non-spherical frictionless particle. Chem. Eng. Sci. 59, 425–435.
Lin, X.S., Ng, T.T., 1995. Contact detection algorithms for three-dimensional ellipsoids in discrete element modelling. Int. J. Numer. Anal. Methods Geomech. 19, 653–659.
Mustoe, G.G.W., Miyata, M., 2001. Material flow analysis of noncircular-shaped granular media using discrete element methods. J. Eng. Mech. 127, 1017–1026.
Müller, C.R., Davidson, J.F., Dennis, J.S., Fennell, P.S., Gladden, L.F., Hayhurst, A.N., Mantle, M.D., Rees, A.C., Sederman, A.J., 2006. Real-time measurement of bubbling phenomena in a three-dimensional gas-fluidized bed using ultrafast Magnetic Resonance Imaging. Phys. Rev. Lett. 96, 154504(4.
Müller, C.R., Davidson, J.F., Dennis, J.S., Fennell, P.S., Gladden, L.F., Hayhurst, A.N., Mantle, M.D., Rees, A.C., Sederman, A.J., 2007a. Oscillations in gas-fluidized beds: ultra-fast magnetic resonance imaging and pressure sensor measurements. Powder Technol. 177, 87–98.
Müller, C.R., Holland, D.J., Davidson, J.F., Dennis, J.S., Gladden, L.F., Hayhurst, A.N., Mantle, M.D., Sederman, A.J., 2007b. Rapid two-dimensional imaging of bubbles and slugs in a three-dimensional, gas-solid, two-phase flow system using ultrafast magnetic resonance. Phys. Rev. E 75, 020302(4.
Müller, C.R., Holland, D.J., Sederman, A.J., Dennis, J.S., Gladden, L.F., 2010. Magnetic resonance measurements of high-velocity particle motion in a three-dimensional gas-solid spouted bed. Phys. Rev. E 82, 050302(4.
Müller, C.R., Holland, D.J., Sederman, A.J., Scott, S.A., Dennis, J.S., Gladden, L.F., 2008. Granular temperature: comparison of magnetic resonance measurements with discrete element model simulations. Powder Technol. 184, 241–253.
Müller, C.R., Scott, S.A., Holland, D.J., Clarke, B.C., Sederman, A.J., Dennis, J.S., Gladden, L.F., 2009. Validation of a discrete element model using magnetic resonance measurements. Particuology 7, 297–306.
Nakagawa, M., Altobelli, S.A., Caprihan, A., Fukushima, E., Jeong, E.-K., 1993. Non-invasive measurements of granular flow by magnetic resonance imaging. Exp. Fluids 16, 54–60.

Third, J.R., Scott, D.M., Scott, S.A., 2010a. Axial dispersion of granular material in horizontal rotating cylinders. Powder Technol. 203, 510–517.
Third, J.R., Scott, D.M., Scott, S.A., Müller, C.R., 2010b. Tangential velocity profiles of granular material within horizontal rotating cylinders modeled using the DEM. Granular Matter 12, 587–595.
Williams, J.R., O'Connor, R., 1995. A linear complexity intersection algorithm for discrete element simulation of arbitrary geometries. Eng. Comput. 12, 185–201.
Williams, J.R., O'Connor, R., 1999. Discrete element simulation and the contact problem. Arch. Comput. Methods Eng. 6, 279–304.
Zhu, H.P., Zhou, Z.Y., Yang, R.Y., Yu, A.B., 2007. Discrete particle simulation of particulate systems: theoretical developments. Chem. Eng. Sci. 62, 3378–3396.
Zhu, H.P., Zhou, Z.Y., Yang, R.Y., Yu, A.B., 2008. Discrete particle simulation of particulate systems: a review of major applications and findings. Chem. Eng. Sci. 63, 5728–5770.